Supporting Information

Activating the S surfaces via Reversing the electron supply direction for fast Hydrogen Sensing

Xin Jia[†a], Musen Li[†b], Yurou Li[a], Panzhe Qiao[c], Xiaowu Wang[a] , Yi Jiang[a], Mengmeng Guo[a], Pengfei Hu[d], Bo Lu[d], Bao-Li An[a] ,Zhenggang Xue[a,] Jiaqiang Xu[a,]**

Table of Contents

1.Experiment detail

1.1 *XAFS Measurements:*

The X-ray absorption fine structure data were collected at 1W1B station in Beijing Synchrotron Radiation Facility (BSRF). The storage rings of BSRF was operated at 2.5 GeV with a maximum current of 250 mA. The X-ray absorption near edge structure (XANES) data were recorded in fluorescence mode. All samples were pelletized as disks of 13 mm diameter using poly(1,1-difluoroethylene) powder as a binder. The acquired extended X-ray absorption fine structure (EXAFS) data were processed according to the standard procedures using the ATHENA module implemented in the IFEFFIT software packages. [1]The EXAFS spectra were obtained by subtracting the post-edge background from the overall absorption and then normalizing with respect to the edge-jump step. Subsequently, $\chi(k)$ data in the k-space were Fourier transformed to real (R) space using a Hanning window (dk = 1.0 $Å^{-1}$) to separate the EXAFS contributions from different coordination shells.

1.2 *Ex situ* XPS experiments:

Ex situ XPS measurements were carried out on X-ray photoelectron spectroscopy (XPS, ESCALAB 250Xi, Thermofisher Scientific) and binding energies were calibrated the of the elements by C 1s (284.6 eV). During the test, the sample was first mounted on a transfer bar and then transferred to the reaction chamber. Next, a gold-plated copper seal was installed to seal the reaction chamber. Then, the target temperature (170^{o}C) is set and the corresponding air is injected for pretreatment for 5 minutes. Finally, the reaction chamber is evacuated, and then transferred directly to the analysis chamber for

testing and analysis. The data obtained is the XPS spectra in air. The reaction chamber was transferred out of the analysis chamber. The corresponding mixture of H_2 gas and air is injected for pretreatment for 5 minutes (H_2 in the gas mixture at a concentration of 2%). Then, the reaction chamber was vacuumed, and then directly transferred to the reaction chamber for testing and analysis. The obtained data is XPS spectra in H_2.

1.3 *In situ Raman experiments*:

The Raman spectra were obtained on a Renishaw spectrometer (Raman, INVIA). The sample was first placed on a silicon wafer in the in-situ reactor. Then a mixture of H_2 gas and air was injected and the Raman spectrum is collected (2% of H_2 in the gas mixture). Finally, data is collected every 30 s and the last data is collected at 150 s to end the test.

1.4 *Gas-sensing measurement:*

The gas-sensitive material was coated on the interdigital electrode of Micro Electro Mechanical System (MEMS) chip. Assembled MEMS sensors were placed onto the bottom of the chamber of LP-002A gas sensing system (Lingpan Electronics Technology Co. Ltd., China). The gas sensing system were shown in Figure S14-S15. The operating voltage of the test circuit is 10 V. The resistance of sensors was obtained by detecting the voltage of the loading resister in series. The resistance (R) of sensor were calculated by the Eq. (1):

$$R = \left(\frac{10 - V_{out}}{V_{out}}\right) \cdot R_L \quad (1)$$

Where 10 is the circuit voltage, V_{out} is the output voltage of the load resistance (R_L) detected. The operating temperature of sensors was achieved by adjusting the heater

57 voltage. When the resistances kept stable, the test gas was injected into the 200 mL
58 chamber. The amount of injected gas can be obtained through the Eq. (2):

59 $$C_x = \frac{V_x}{200} \cdot C \quad (2)$$

60

61 Where V_x(mL) is the gas volume extracted from the gas sampling bags by the micro
62 syringe, 200 is the volume of the test chamber, C is the standard concentration of gas
63 in gas sampling bags and the C_x is the different gas concentration in the test chamber.
64 The response value of sensors in a reducing atmosphere is defined as response = R_a/R_g.
65 The resistance of the sensor in the air is recorded as R_a and that in the test gas is R_g.

66 The selectivity coefficient (K) can be used to quantitatively assess the selectivity of the
67 sensor. The K value can be calculated by the Eq. (3):

68 $$K = \frac{response_{SO2}}{response_x} \quad (3)$$

69 where the response SO_2 is the response of the sensor in 5 ppm SO_2 and the response x
70 is the response of the sensor in 5 ppm other gases.

71 **1.5 *Gas (H_2) Adsorption and Desorption Tests:***

72 The Quartz crystal microbalance (QCM) resonators were purchased from Chengdu
73 West Sensor Technology Co., Ltd. QCM measurement is composed of a thin slice of
74 quartz crystal with double-faced deposited silver electrodes. The mechanism of QCM

is based on the piezoelectric effect of quartz crystal oscillator, where there is a quantitative relationship between the increasing mass change (Δm) and decreasing frequency change (Δf). The quantitative relationship is in accordance with the Sauerbrey equation: $\Delta f=-2.3\times10^{-6}\times f_0^2\Delta m/A$. Where f_0 is the inherent oscillation frequency of the chip (10^7, Hz), A is the effective working area of the electrodes (d=3 mm).

1.6 ***Methodology and calculation model:***

All DFT computations were performed in the Vienna ab initio simulation package (VASP) [2] under projector augmented wave (PAW) potentials to describe the interactions. The generalized gradient approximation (GGA) [3] in the Perdew–Burke–Ernzerhof (PBE) functional was used to treat the exchange-correlation between electrons. The way of DFT-D3 [4] was adopt to correct van der Waals force. A cut-off energy of 500 eV for plane wave expansions was used and all geometric structures were set a 10 Å vacuum layer in the z-direction. The 10^{-5} eV for conventional energy and 0.02 eV $Å^{-1}$ for force under a 2×2×1 sheet k-point mesh were taken as the convergence criteria to optimize the structures. The electronic structures of the density of state (DOS) were calculated with 3×3×1 k-points. In all of the structure optimization, the bottom half of the slab in the vertical z-direction was constrained, while the top half of the slab and the adsorbates were fully relaxed. In this calculation, the ZnS (0 0 2) was modeled by a 2×2 supercell. The adsorption energy (ΔE) of H_2 on the substrates can be given by Eq. (4):

$$\Delta E=E_{total}-E_{H2}-E_{substrate} \quad (4)$$

Where E_{total}, E_{H2}, and $E_{substrate}$ are the energy of H_2 adsorption on the substrate, energy of H_2, and energy of substrate, respectively.

2. Supporting Figures and Tables

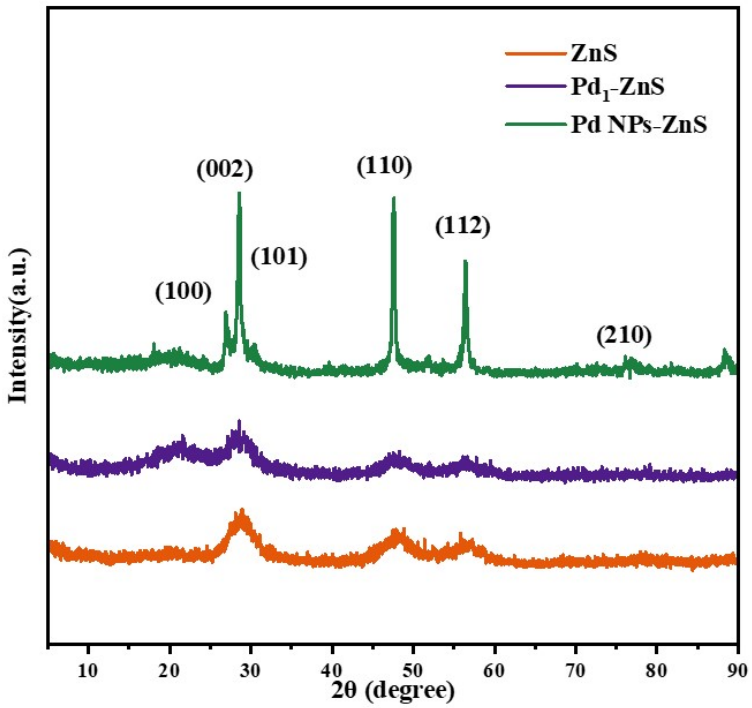

Fig. S1. XRD pattern of the ZnS, Pd_1-ZnS and Pd NPs-ZnS.

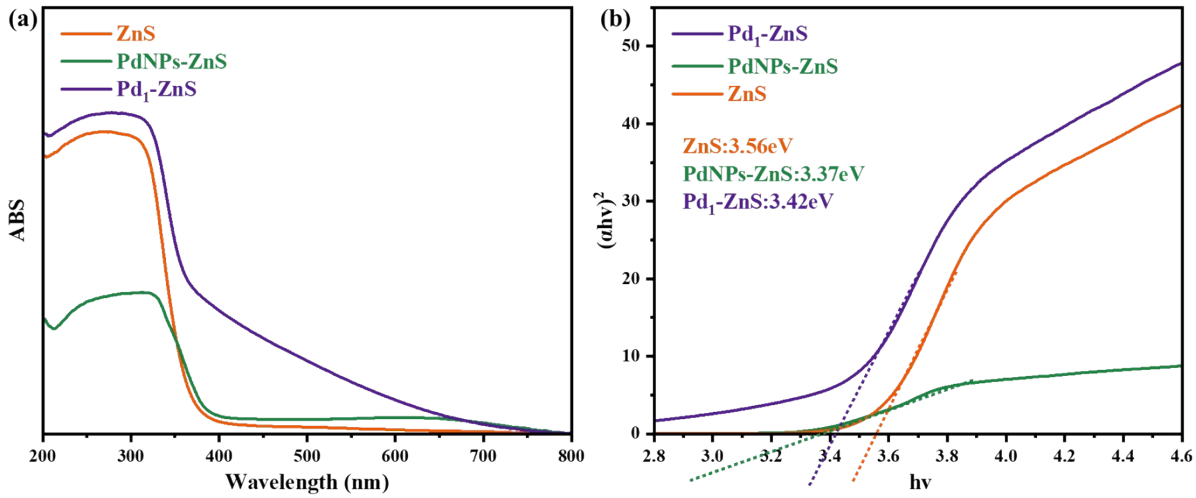

Fig. S2. (a) UV-vis diffuse reflectance spectrum and (b) Kubelka-Munk function curve plotted against photon versus the energy of absorbed light of ZnS, Pd_1-ZnS and Pd NPs-ZnS.

The relationship between $(\alpha hv)^2$ and photon energy hv is obtained according to the formula $(\alpha hv)^2 = A (hv\text{-}Eg)$, where α, A, h and v are the absorption coefficient, absorption constant, Plank constant and light frequency, respectively. Extrapolate the part of the spectra near the absorption edge, the intersection with the abscissas is obtained.

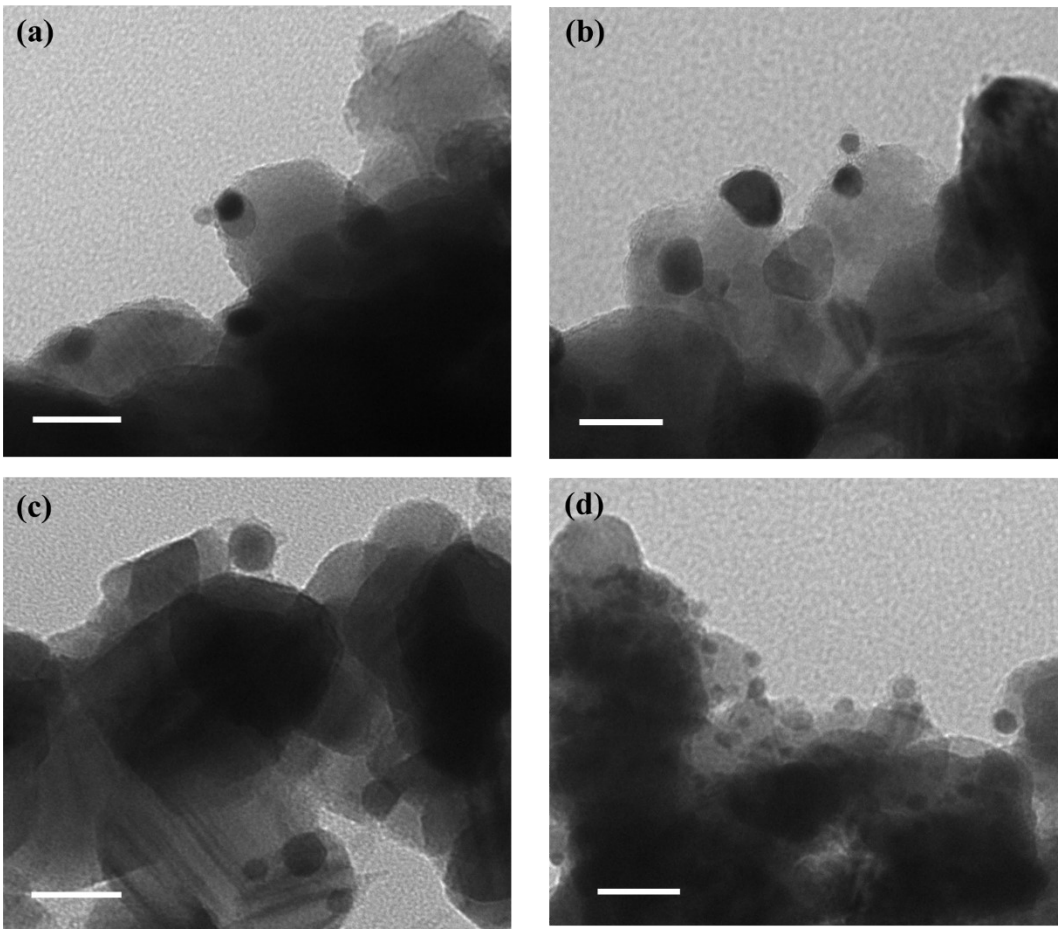

Fig. S3. TEM images of Pd NPs-ZnS, scale bar is 25 nm.

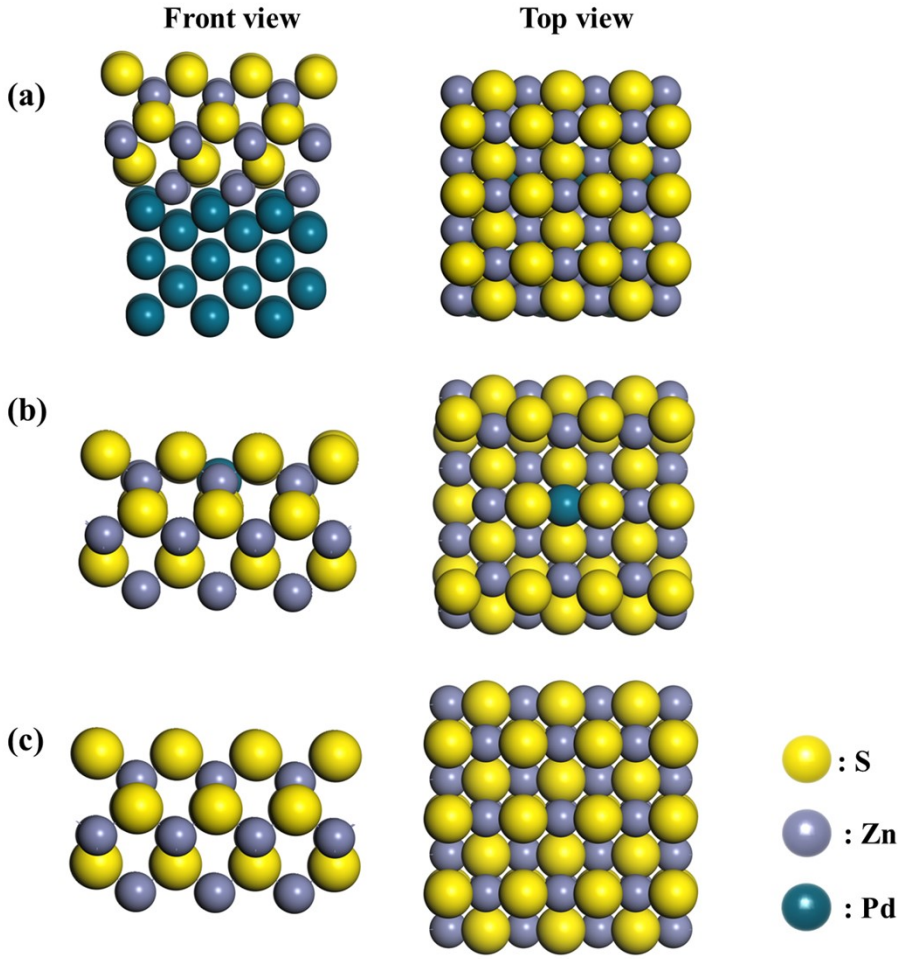

Fig. S4. Structure models for (a) Pd NPs-ZnS (b) Pd_1-ZnS (c) ZnS.

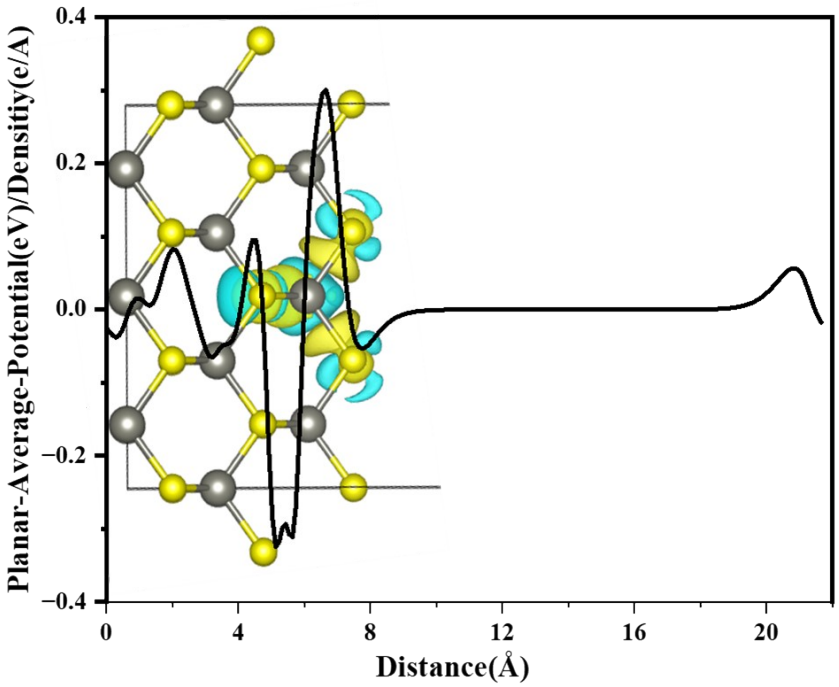

Fig. S5. The planar-averaged electron density difference Δρ(z) of Pd_1-ZnS.

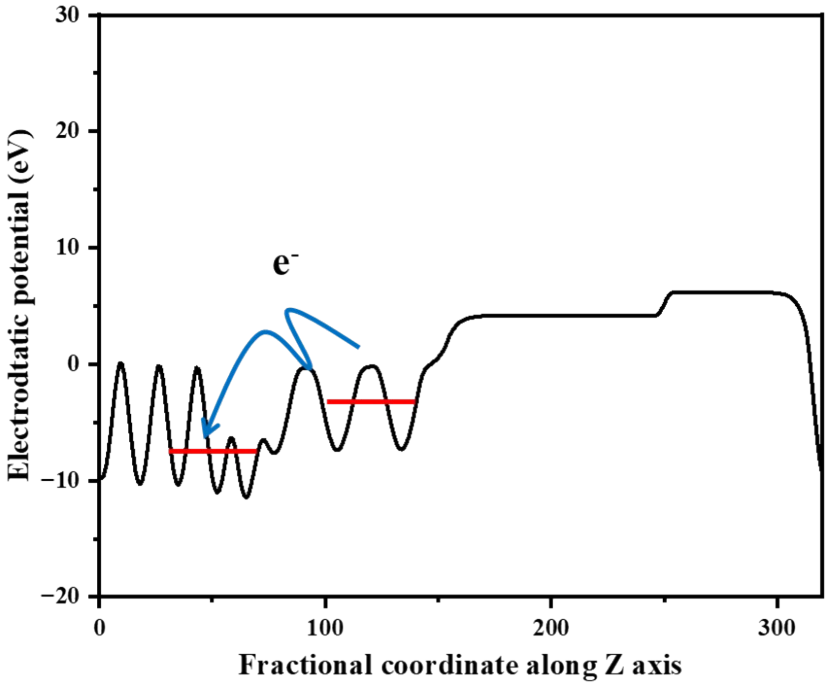

Fig. S6. Work functions of Pd NPs-ZnS.

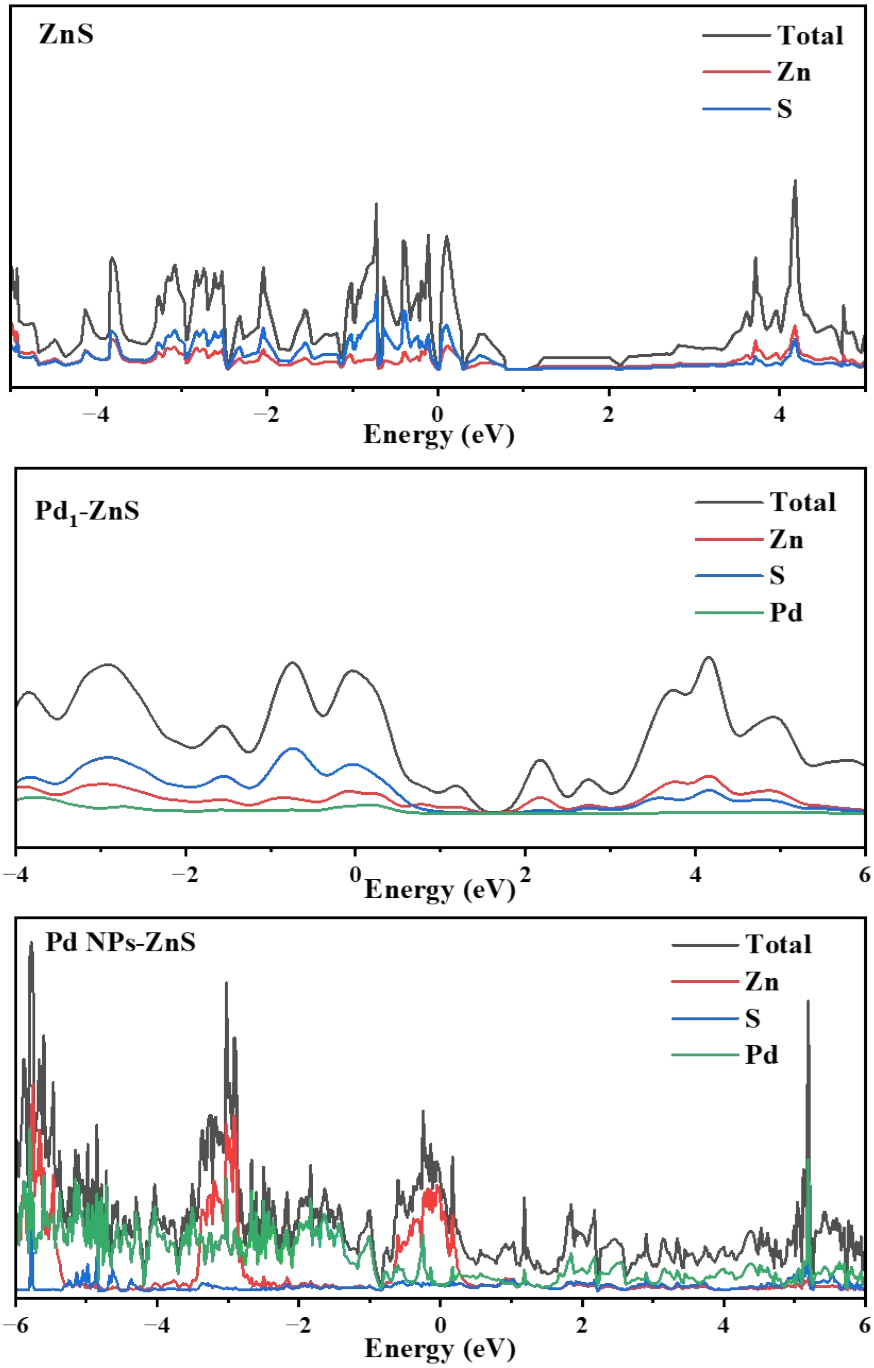

Fig. S7. The total density of states (TDOS) and projected density of state (PDOS) of ZnS, Pd_1-ZnS and Pd NPs-ZnS.

When electrons flow into a material, the Fermi-level of the material will increase, and when electrons flow out, the Fermi-level of the material will decrease.

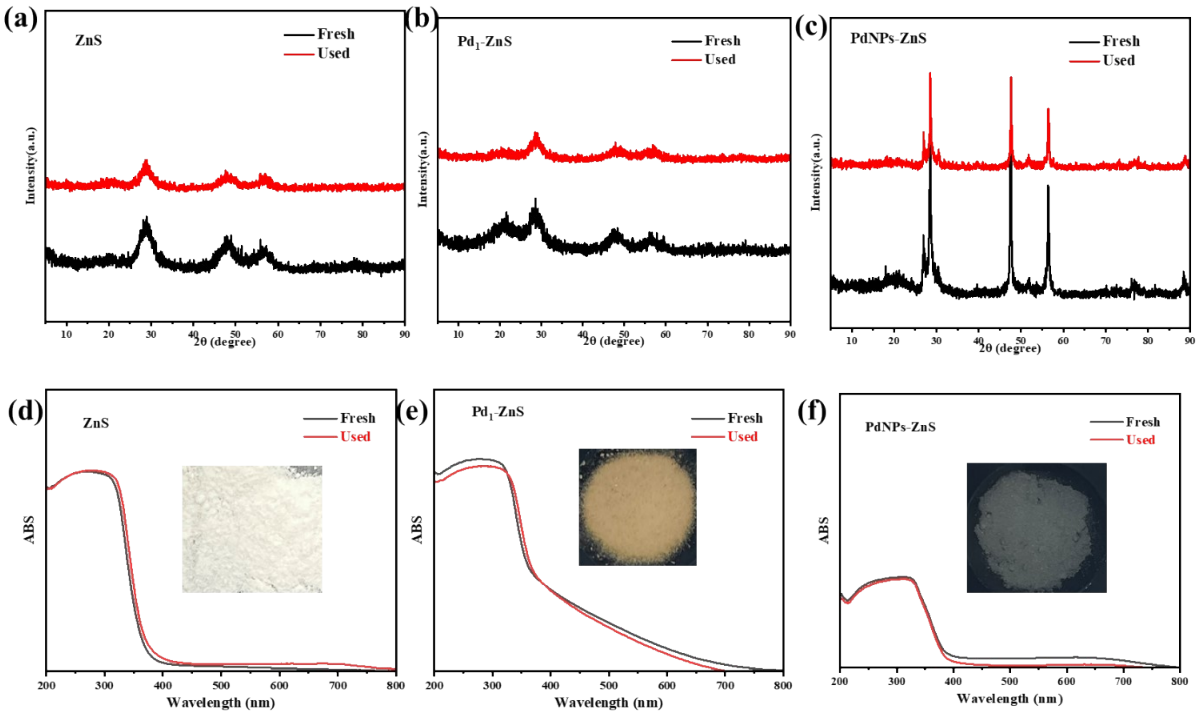

133

134 **Fig. S8.** (a-c) XRD pattern of the ZnS and ZnS after 200℃ for 2h, Pd_1-ZnS and Pd_1-
135 ZnS after 170℃ for 2h, Pd NPs-ZnS and Pd NPs-ZnS after 200℃ for 2h. (d-f) UV-vis
136 diffuse reflectance spectra of the ZnS and ZnS after 200℃ for 2h, Pd_1-ZnS and Pd_1-
137 ZnS after 170℃ for 2h, Pd NPs-ZnS and Pd NPs-ZnS after 200℃ for 2h.

138 XRD and UV-vis spectra show that the three materials can maintain the corresponding
139 crystal structure at the corresponding optimum operating temperature.

140

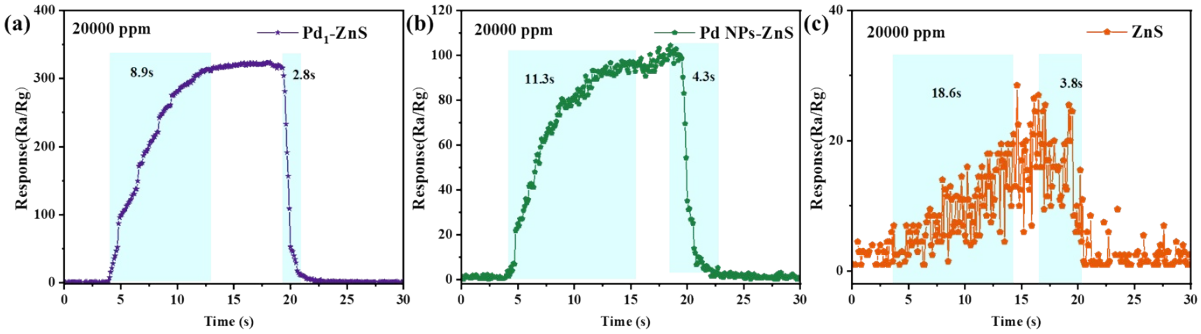

Fig. S9. Response transient of the Pd1-ZnS, Pd NPs-ZnS and ZnS sensors to 20000 ppm H_2.

The response and recovery times of the Pd NPs-ZnS (11.3 s/4.3 s for 20000 ppm) and ZnS (18.6s/3.8s for 20000 ppm) sensors are all longer than the response and recovery times of Pd_1-ZnS sensors (8.9s/2.9s for 20000 ppm).

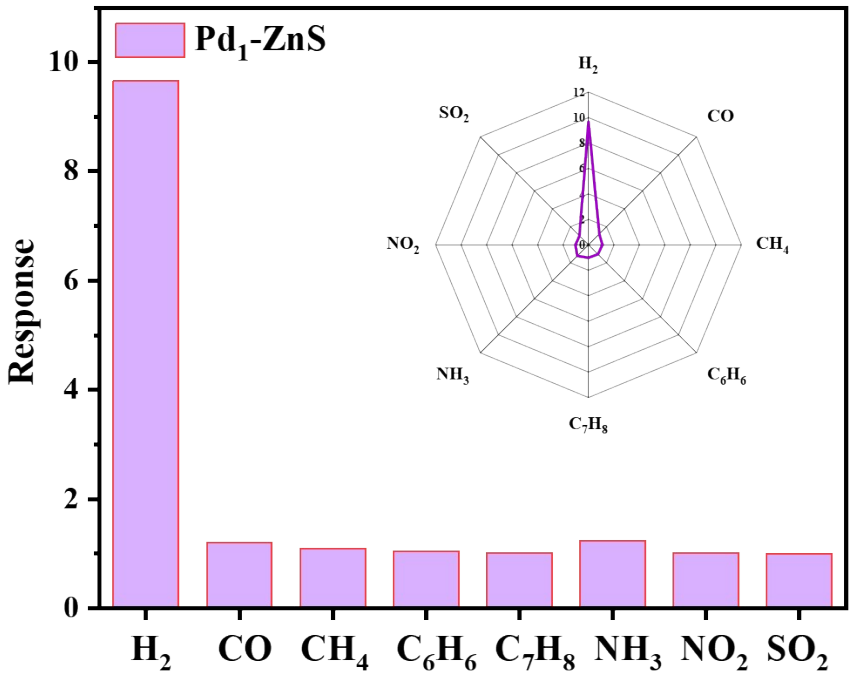

Fig. S10. Selectivity of Pd_1-ZnS sensors towards 20 ppm various gas species.

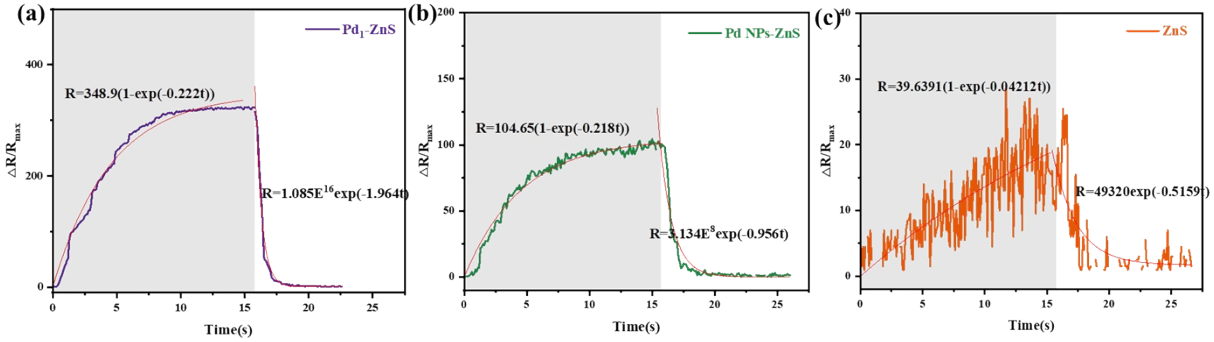

Fig. S11. Dynamic response transitions and the corresponding response/recovery fitting curves of the sensors for 20000 ppm of H_2 sensing.

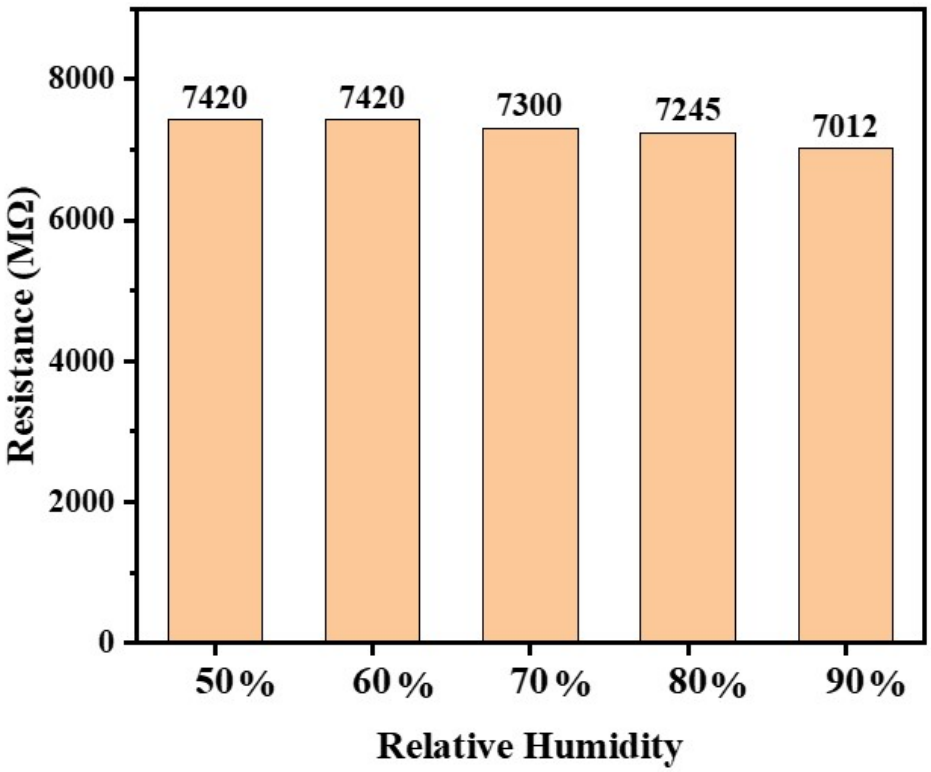

Fig. S12. Baseline resistance at different relative humidity of Pd1-ZnS in air.

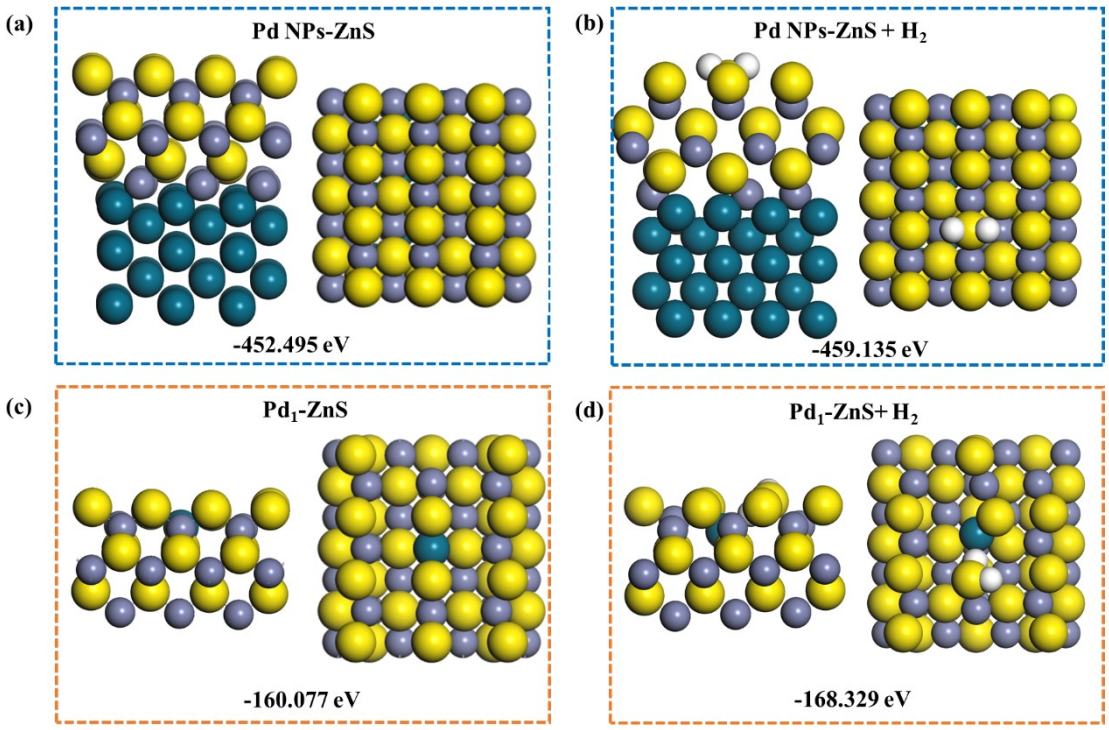

163

164 **Fig. S13.** Optimized models of the adsorption of the H_2 molecules and energies on Pd_1-
165 ZnS and Pd NPs-ZnS.

166

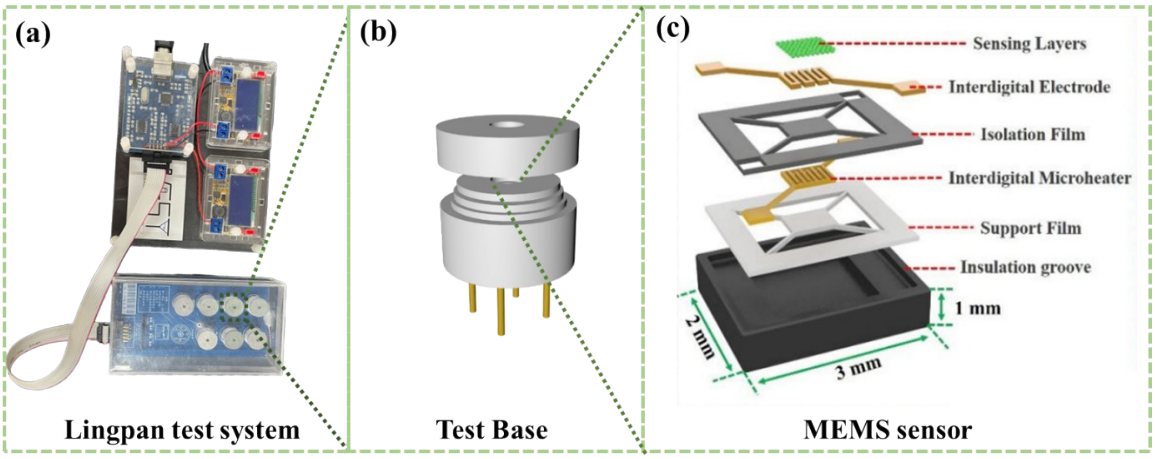

Fig. S14. Schematic of the fabrication for gas sensing system. (a) the gas sensing system LP-002A, (b) the exploded views of test base, (c) MEMS sensors.

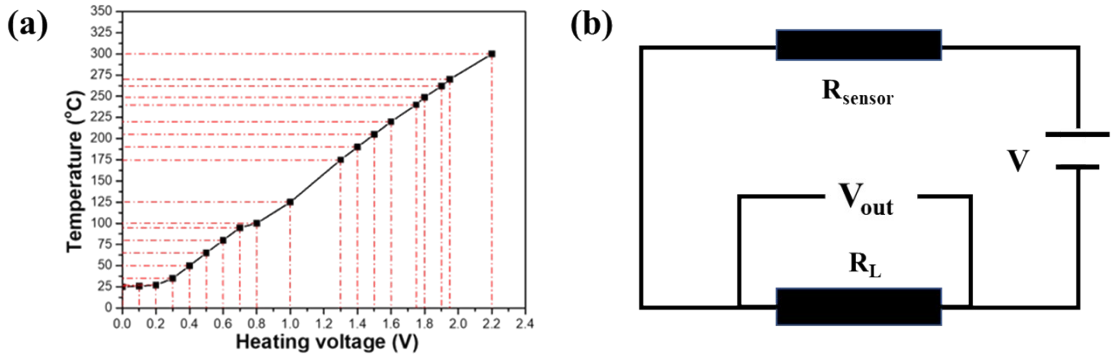

172

173 **Fig. S15.** (a) The relationship between the temperature and the voltage of MEMS gas
174 sensors, (b)measuring circuit of MEMS sensors.

175

TableS1. EXAFS fitting parameters at the Pd *K*-edge for various samples*.

Sample	Shell	*CN*[a]	*R*(Å)[b]	σ^2(Å^2)[c]	ΔE_0(eV)[d]	*R* factor
Pd foil	Pd-Pd	12	2.74			0.002
PdO	Pd-O	4.0	2.02			0.009
	Pd-Pd1	4.0	3.02			
	Pd-Pd2	8.0	3.41			
Pd_1-ZnS	Pd-S	4.3	2.34	0.0027	-6.3	0.004

[a]*CN*, coordination number; [b]*R*, the distance to the neighboring atom; [c]σ^2, the Mean Square Relative Displacement (MSRD); [d]ΔE_0, inner potential correction; *R* factor indicates the goodness of the fit. *This value was fixed during EXAFS fitting, based on the known structure of Pd. Fitting range: 2.6 $\leq k$ (/Å) $\leq$ 12.7 and 1.4 $\leq R$ (Å) $\leq$ 3.0 (Pd foil), 2.5 $\leq k$ (/Å) $\leq$ 12.4 and 1.0 $\leq R$ (Å) $\leq$ 3.6 (PdO), 2.6 $\leq k$ (/Å) $\leq$ 10.6 and 1.2 $\leq R$ (Å) $\leq$ 2.2 (Pd_1-ZnS).

Table S2. The content of noble metals in the obtained composites was measured by ICP-OES.

Samples	Zn (μg/ml)	Pd (μg/ml)	Content of Pd (wt%)
Pd_1-ZnS	8.308	0.0379	0.45
Pd NPs-ZnS	7.024	0.0368	0.52

Table S3. The summary of the response time(τ_{res}) of the sensors for the H_2 (1 ppm) sensing reaction.

Operating Temperature/℃·K^{-1}	Response time/s		
	ZnS	Pd1-ZnS	Pd NPs-ZnS
140/413	12.25	7.52	11.25
150/423	11.78	6.35	10.25
160/433	10.48	6.27	9.55
170/443	10.48	5.42	8.95
180/453	9.45	5.02	8.34
200/473	6.43	/	6.52
220/493	5.13	/	5.22

When the obtained sensor response kinetics is governed by the adsorption process, the relaxation time (τ_{res}) can be written as a function of temperature according to the well-known thermal activation function.

$$\tau_{res} = \tau_0 exp(E_{act}/RT)$$

$$ln^{\tau_{res}} = ln^{\tau_0} + E_{act}/RT$$

$$Slope = E_{act}/R$$

Here, where τ_0 is the pre-exponential constant, which is determined only by the nature of the reaction and independent of the reaction temperature and gas concentration in the system; T is the working temperature (K) and R is the universal gas constant (8.314 J·mol·K^{-1}); E_{act} is the activation energies.

Table S4. The of QCM tests.

Sample	Fundamental frequency (10^6 hz)	Frequency after coating (10^6 hz)	Frequency shift (hz)	Load mass (ng)
ZnS	10003080.9	9998001.4	5079.5	2821.9
Pd NPs-ZnS	10002847.2	10002518.7	328.5	182.5
Pd_1-ZnS	10002986.1	10002704.2	281.9	156.61

Table S5. The summary of the reaction rate constants of ZnS, Pd_1-ZnS and Pd NPs-ZnS.

Sample	K_{ads} ($ppm^{-1}S^{-1}$)	Kdes (S^{-1})	K (K_{ads} / Kdes ppm^{-1})
ZnS	$1.298*10^{-6}$	0.516	$2.516*10^{-6}$
Pd NPs-ZnS	$9.164*10^{-7}$	0.956	$9.586*10^{-7}$
Pd_1-ZnS	$2.465*10^{-6}$	1.964	$1.255*10^{-6}$

Table S6. The reported H_2 sensors and their gas sensing performances.

Sensing material	H_2 Conc. (ppm)	Operating temperature (°C)	Response (R_a/R_g)	LOD (ppm)	Response/ recovery times	Ref.
Pd-SnO_2 nanosheets	100	200	33	0.45	10 s/62 s	[5]
ZnO/ZnS core-shell	1000 ppm	300	20%	500	/	[6]
ZnO NFs	10	350	150	0.1	>2 min/>5 min	[7]
Pd/SnO_2 nanowires	100	150	4.5	1	> 5 min/ > 6 min	[8]
Pd/ZnO–SnO_2 NFs	200	270	171	0.25	1 s/20 s	[9]
0.2%Pt-SnO_2 nanoparticles	1%	200	150.2	200	60s/120s	[10]
Pd nanopattern	1000	25	1.5%	2.5	12s/30s	[11]
Hollow Pd−Sn alloy nanotubes	200	25	1.63%	1	20/18	[12]
Pd single-atom-Co_3O_4	1000	125	80	/	15s/70s	[13]
1.5%Pd/ZnO	100	360	11.3	5	2s/5s	[14]
Pd/SiC	100	380	14.48	5	10/18	[15]
Pd-Au NDs/In_2O_3 NCBs	500	280	45	0.3	5/3	[16]
PdO/WO_3	10	150	76	5	5/113	[17]
Pd_1-ZnS	**400**	**170**	**70.66**	**20**	**5.1/1.8**	**This work**

Reference:

1 X. Wang, W. Chen, L. Zhang, T. Yao, W. Liu, Y. Lin, H. Ju, J. Dong, L. Zheng, W. Yan, X. Zheng, Z. Li, X. Wang, J. Yang, D. He, Y. Wang, Z. Deng, Y. Wu and Y. Li, *J. Am. Chem. Soc.*, 2017, **139**, 9419–9422.

2 G. Kresse and J. Furthmüller, *Phys. Rev. B*, 1996, **54**, 11169–11186.

3 J. P. Perdew, K. Burke and M. Ernzerhof, *Phys. Rev. Lett.*, 1996, **77**, 3865–3868.

4 S. Grimme, J. Antony, S. Ehrlich and H. Krieg, *J. Chem. Phys.*, 2010, **132**, 154104.

5 G. Li, Y. Fan, Q. Hu, D. Zhang, Z. Ma, Z. Cheng, X. Wang and J. Xu, *J. Alloys Compd.*, 2022, **906**, 163765.

6 Y.-S. Tsai, T.-W. Chou, C. Y. Xu, W. Chang Huang, C. F. Lin, Y. S. Wu, Y.-S. Lin and H. Chen, *Ceram. Int.*, 2019, **45**, 17751–17757.

7 J.-H. Kim, A. Mirzaei, H. Woo Kim, P. Wu and S. S. Kim, *Sens. Actuators B Chem.*, 2019, **293**, 210–223.

8 Z. Cai and S. Park, *Sens. Actuators B Chem.*, 2020, **322**, 128651.

9 K. Hu, F. Wang, Z. Shen, H. Liu and J. Xiong, *J. Alloys Compd.*, 2021, **850**, 156663.

10 C. Liewhiran, N. Tamaekong, A. Wisitsoraat, A. Tuantranont and S. Phanichphant, *Sens. Actuators B Chem.*, 2013, **176**, 893–905.

11 S.-Y. Cho, H. Ahn, K. Park, J. Choi, H. Kang and H.-T. Jung, *ACS Sens.*, 2018, **3**, 1876–1883.

12 L. Song, J. Ahn, D.-H. Kim, H. Shin and I.-D. Kim, *ACS Appl. Mater. Interfaces*, 2022, **14**, 28378–28388.

13 K. Koga, *ACS Appl. Mater. Interfaces*, 2020, **12**, 20806–20823.

14 J. Gao, B. Wu, C. Cao, Z. Zhan, W. Ma and X. Wang, *ACS Sustain. Chem. Eng.*, 2021, **9**, 6370–6379.

15 A. Kumar, A. Kumar and R. Chandra, *Sens. Actuators B Chem.*, 2018, **264**, 10–19.

16 X. Zhao, L. Du, X. Xing, Z. Li, Y. Tian, X. Chen, X. Lang, H. Liu and D. Yang, *Small*, **n/a**, 2311840.

17 L. Cai, S. Zhu, G. Wu, F. Jiao, W. Li, X. Wang, Y. An, Y. Hu, J. Sun, X. Dong, J. Wang, Q. Lu, Q. Jing and B. Liu, *Int. J. Hydrog. Energy*, 2020, **45**, 31327–31340.